Monocyte-directed RNAi targeting CCR2 improves infarct healing in atherosclerosis-prone mice

Published in final edited form as:
Circulation. 2013 May 21; 127(20): 2038–2046. doi:10.1161/CIRCULATIONAHA.112.000116.

Monocyte-directed RNAi targeting CCR2 improves infarct healing in atherosclerosis-prone mice

Maulik D. Majmudar, M.D.[1], **Edmund J. Keliher, Ph.D.**[1], **Timo Heidt, M.D.**[1], **Florian Leuschner, M.D.**[1], **Jessica Truelove, BS**[1], **Brena F. Sena, BS**[1], **Rostic Gorbatov, BS**[1], **Yoshiko Iwamoto, BS**[1], **Partha Dutta, Ph.D.**[1], **Gregory Wojtkiewicz, MS**[1], **Gabriel Courties, Ph.D.**[1], **Matt Sebas, BS**[1], **Anna Borodovsky, Ph.D.**[2], **Kevin Fitzgerald, Ph.D.**[2], **Marc W. Nolte, Ph.D.**[3], **Gerhard Dickneite, Ph.D.**[3], **John W. Chen, M.D., Ph.D.**[1], **Daniel G. Anderson, Ph.D.**[4,5,6], **Filip K. Swirski, Ph.D.**[1], **Ralph Weissleder, M.D., Ph.D.**[1,7], and **Matthias Nahrendorf, M.D., Ph.D.**[1]

[1]Center for Systems Biology, Massachusetts General Hospital, Boston, MA

[2]Alnylam Pharmaceuticals, Cambridge, MA, USA

[3]CSL Behring GmbH, Marburg, Germany

[4]David H. Koch Institute for Integrative Cancer Research, Massachusetts Institute of Technology, Cambridge, MA, USA

[5]Department of Chemical Engineering, MIT

[6]Division of Health Science Technology, MIT

[7]Department of Systems Biology, Harvard Medical School, Boston, MA

Abstract

Background—Exaggerated and prolonged inflammation after myocardial infarction (MI) accelerates left ventricular remodeling. Inflammatory pathways may present a therapeutic target to prevent post-MI heart failure. However, the appropriate magnitude and timing of interventions are largely unknown, in part because noninvasive monitoring tools are lacking. We here employed nanoparticle-facilitated silencing of CCR2, the chemokine receptor that governs inflammatory Ly-6C^{high} monocyte subset traffic, to reduce infarct inflammation in apoE$^{-/-}$ mice after MI. We used dual target PET/MRI of transglutaminase factor XIII (FXIII) and myeloperoxidase (MPO) activity to monitor how monocyte subset-targeted RNAi altered infarct inflammation and healing.

Methods and Results—Flow cytometry, gene expression analysis and histology revealed reduced monocyte numbers and enhanced resolution of inflammation in infarcted hearts of apoE$^{-/-}$ mice that were treated with nanoparticle-encapsulated siRNA. To follow extracellular matrix crosslinking non-invasively, we developed a fluorine-18 labeled PET agent (^{18}F-FXIII). Recruitment of MPO-rich inflammatory leukocytes was imaged using a molecular MRI sensor of MPO activity (MPO-Gd). PET/MRI detected anti-inflammatory effects of intravenous nanoparticle-facilitated siRNA therapy (75% decrease of MPO-Gd signal, $p<0.05$) while ^{18}F-FXIII PET reflected unimpeded matrix crosslinking in the infarct. Silencing of CCR2 during the first week after MI improved ejection fraction on day 21 after MI from 29 to 35% ($p<0.05$).

Address for correspondence: Matthias Nahrendorf Center for Systems Biology Massachusetts General Hospital 185 Cambridge St Boston, MA, 02114 Phone: 617-935-9177 Fax: 617-643-6133 mnahrendorf@mgh.harvard.edu.

Disclosures Anna Borodovsky and Kevin Fitzgerald are employees at Alnylam. Daniel Anderson holds Alnylam shares. Marc W. Nolte and Gerhard Dickneite are employees of CSL Behring GmbH and own employee shares of CSL Limited.

Conclusion—CCR2 targeted RNAi reduced recruitment of Ly-6C^{high} monocytes, attenuated infarct inflammation and curbed post-MI left ventricular remodeling.

Keywords

myocardial infarction; remodeling; monocytes; RNAi; PET/MRI

INTRODUCTION

Infarct healing is a complex biological process that occurs during the first 2 weeks after myocardial infarction (MI)[1-3]. The quality of healing influences outcome, as impaired healing leads to infarct expansion and accelerated left ventricular remodeling[4, 5]. Monocytes and macrophages are innate immune cells which pursue cardinal functions in infarct healing, for instance removal of dead tissue through phagocytosis and release of proteases[6]. Inflammatory leukocytes may also oppose wound healing[7]. In the setting of atherosclerosis, hematopoiesis in the bone marrow and spleen supplies excessive numbers of these cells[8]. Here, monocyte recruitment to the infarct increases beyond necessary levels, counteracting resolution of inflammation in later healing stages[7, 9]. Resolution of inflammation, however, supports ensuing reparative processes in the infarct[6]. Prolonged presence of inflammatory leukocytes in the cardiac wound may counteract the build-up of new extracellular matrix that guarantees the stability of the infarct scar and the left ventricle[1-3, 10].

Inflammatory Ly-6C^{high} monocytes depend on the chemokine/chemokine receptor pair MCP-1/CCR2 to travel to the site of inflammation[9, 11]. We previously developed an approach to selectively target recruitment of Ly-6C^{high} monocytes by *in vivo* silencing of the chemokine receptor CCR2[12]. Using lipidoid nanoparticles as delivery vehicles, RNAi targeting of CCR2 reduced mRNA and protein levels of the receptor in Ly-6C^{high} monocytes and consequently curtailed their accumulation to the site of inflammation[12]. This anti-inflammatory strategy does not directly affect recruitment of the reparative Ly-6C^{low} monocyte subset which relies on fractalkine/CX3CR1, or resident cells involved in wound repair.

Here we used RNAi to decrease Ly-6C^{high} monocyte recruitment during infarct healing. Ligating the coronary artery in apoE$^{-/-}$ mice, we modeled the situation of patients that experience myocardial ischemia due to hypercholesterolemia and atherosclerosis[7]. We assessed infarct healing with *in vivo* hybrid imaging to follow two key aspects of wound repair which reflect antagonistic aspects of tissue remodeling. Inflammation, which dominates the cardiac wound early after ischemia and may become destructive if it does not resolve swiftly, was quantified with a myeloperoxidase-activatable gadolinium-based MRI agent (MPO-Gd)[13]. Extracellular matrix synthesis and organization are important components of infarct healing and left ventricular remodeling that may be altered by anti-inflammatory interventions. Crosslinking of extracellular matrix, a hallmark of these reparative processes[14], was assessed with a newly developed fluorine-18 PET imaging agent for transglutaminase activity (^{18}F-FXIII). Monitoring the therapeutic effect of *in vivo* RNAi with the first dual-target molecular cardiac PET/MRI study, we tested the hypothesis that silencing of CCR2 in Ly-6C^{high} monocytes after MI improves infarct healing and attenuates left ventricular remodeling.

METHODS

^{18}F-FXIII probe synthesis

Enzymatic activity of plasma transglutaminase factor XIII (FXIII) in the infarct was assessed with a fluorine-18 labeled affinity peptide (^{18}F-FXIII), which the enzyme

recognizes as a substrate and then cross-links to extracellular matrix proteins[14]. Thus, local entrapment of the PET isotope linked to the peptide correlates to the crosslinking activity of the enzyme. Based on previous work with the peptide[14, 15], we here developed and validated a PET agent for PET/MRI of infarct healing. Synthesis of ^{18}F-FXIII involved cycloaddition chemistry between tetrazine and transcyclooctyne (Figure 1A), as previously developed for facile and rapid production of peptide based PET agents[16, 17].

The custom synthesized FXIII peptide (9.1 mg, 5.5 μmol, sequence: ACGNQEQVSPLTLLKW, Genscript) was dissolved in dimethylsulfoxide (DMSO) and reacted with 2,5-dioxopyrrolidin-1-yl 5-(4-(1,2,4,5-tetrazin-3-yl)benzylamino)-5-oxopentanoate (Tz-NHS) and triethylamine[18]. After stirring at room temperature for 1 hour, HPLC purification was performed on a Waters liquid chromatography mass spectrometry system equipped with an Atlantis® Prep T3 OBD^{TM} 5 μM column to give 7.1 mg of the click reaction precursor FXIII-tetrazine (FXIII-Tz). Analysis by liquid chromatography-electrospray ionisation-mass spectrometry (LC-ESI-MS) was conducted using a Waters XTerra® C18 5 μm column: LC-ESI-MS(+) *m*/*z* (%) = 698.7 (100), 996.7 $(M+2H)^{2+}$ (57), 1937.8 $(M+H)^{1+}$ (9); LC-ESI-MS(-) *m*/*z* (%) = 967.4 (100), 1935.8 $(M-H)^{1-}$ (26).

2-(^{18}F)-(*E*)-5-(2-Fluoroethoxy)cyclooct-1-ene (^{18}F-TCO, 344 MBq, 9.3 ± 5.6 mCi, n = 14) was prepared as previously described[16, 19] by nucleophilic substitution with azeotropically dried (^{18}F)-F^- (n.c.a., 3145 MBq, 85 ± 29 mCi) tetrabutylammonium bicarbonate (18.8 μmol) and (E)-2-(cyclooct-4-enyloxy)ethyl 4-methylbenzenesulfonate (2.0 mg, 12.3 μmol) in 56 ± 19% decay-corrected radiochemical yield (n = 14). Analytical HPLC demonstrated >94% radiochemical purity for the second click reaction precursor ^{18}F-TCO.

FXIII-Tz (25 nmol, 1 mM in DMSO) was then added to ^{18}F-TCO (344 MBq, 9.3 ± 5.6 mCi, n = 14) in DMSO. The reaction mixture was subjected to HPLC purification (Machery Nagel VarioPrep Nulceodur C18 Pyramid column, isocratic 62.4/37.5/0.1% water/ acetonitrile/trifluoracetic acid). Evaporation of HPLC solvents provided 2.8 (104 MBq) ± 1.9 mCi of ^{18}F-FXIII in 57.6 ± 21.2% decay-corrected radiochemical yield (n = 14) and 95 ± 3% radiochemical purity.

MPO agent synthesis

The synthesis of the MPO-specific MRI agent bis-5-hydroxytryptamide-diethylenetriamine-pentaacetate gadolinium (bis-5HT-DTPA(Gd), MPO-Gd, molecular weight = 863 g/mol) was described previously[20, 21]. In brief, 100 mg (0.28 mmol) of DTPA-bisanhydride was reacted with serotonin (Alfa Aesar, Ward Hill, MA) in dimethylformamide (4 mL) in the presence of 100 μL (1 mmol) of pyridine and 50 mg (2.8 mmol) of ascorbic acid. The mixture was then stirred for 30 minutes at room temperature. The crude product was subsequently precipitated with ether, dissolved in water and passed through a C18 cartridge with water and acetonitrile mixtures. The synthesis of corresponding Gd^{3+} complexes was performed in a 5% citric acid solution (pH=5.0) at room temperature. GdCl3•6H2O was used in excess (1.5-fold) in comparison to the chelates and the reaction was stirred for 1 hour. The final product was purified using HPLC (water/acetonitrile) with peak detection at 280 nm. The purity of the agent was confirmed by mass spectrometry and final yield was 30%. Activation of MPO-Gd by myeloperoxidase increases molecular size and the activated sensor can bind to proteins, resulting in increased and prolonged high signal intensity in areas of elevated myeloperoxidase activity[13, 21-23].

Animal models

Female C57Bl/6 (B6; n=20) and apolipoprotein E ($apoE^{-/-}$) mice (n=46) were purchased from the Jackson Laboratory (Jackson) and male $FXIII^{-/-}$ mice (n=30) were provided by

CSL Behring (Marburg, Germany). ApoE$^{-/-}$ mice had an average age of 30 weeks and were fed a high-cholesterol diet (HCD; Harlan Teklad, 0.2% total cholesterol) for at least 16 weeks. Mice were anesthetized for all procedures (isoflurane 1.5%; O_2 2 L/min). All animal experiments were approved by Massachusetts General Hospital's Institutional Subcommittee on Research Animal Care.

Myocardial infarction was induced by permanent coronary ligation[7]. Mice were anesthetized with isoflurane, intubated and ventilated. Left thoracotomy was performed in the fourth intercostal space. The left ventricle was visualized and the left anterior descending coronary artery was permanently ligated with monofilament 8-0 suture (Ethicon, Somerville, NJ). The chest wall was closed with 7-0 nylon sutures and the skin was sealed with glue.

Mice were randomly assigned to a treatment cohort on the day following myocardial infarction. Mice were treated with 0.5 mg/kg/day of siRNA against CCR2 (siCCR2) or control siRNA (siCON) via tail vein injections on days 1, 3, and 5 after induction of MI. Imaging was performed on day 4 (dual target PET/MRI) and day 21 after MI (MR volumetry). Hearts were harvested from additional cohorts for *ex vivo* flow cytometric analysis and gene expression analysis on day 4, whereas histology of wound healing parameters was performed on day 7 after MI. To determine the source of FXIII in the infarct, we depleted circulating monocytes by injecting mice in a separate cohort with i.v. 0.1 mL of dichloromethylene-bisphosphonate liposomes, previously shown to be effective in the setting of coronary ligation[9], on day 3 after MI and harvested hearts for assessment of FXIII activity on day 4.

PET/MRI

We performed *in vivo* PET/MRI on day 4 after MI in apoE$^{-/-}$ mice treated with siCCR2 or siCON. To obtain cardiac PET/MRI, we used separate PET/CT and MRI systems followed by offline data fusion, facilitated by a custom-designed mouse bed and a PET-CT gantry adapter[7]. Fiducial markers aided data fusion, consisting of a custom-built mouse vest made of PE50 loops filled with 15% iodine in water, rendering them visible in both CT and MRI. PET data were fused to CT as part of a standard PET-CT workflow. Registration of MRI and CT data sets was obtained as previously described[24].

PET/CT was acquired on a Siemens Inveon. Mean injected activity was 313 ± 71 μCi/mouse and each acquisition was ~90 minutes in duration. PET was reconstructed from 600 million coincidental 511 keV photon counts. A reconstruction of sinograms yielded a 3D mapping of positron signal using fourier rebinning and a 2D filtered back-projection algorithm with a ramp filter. Voxel size was 0.80 × 0.86 × 0.86mm. Data were expressed as standard uptake values (SUV), which normalizes activity for body weight and injected activity. Computed Tomography (CT) images were obtained using an 80 kVp 500 mA x-ray tube anode on a solid state detector within 10 minutes. CT images were reconstructed using a modified Feldkamp cone beam reconstruction algorithm (COBRA) from 360 projections into an isotropic pixel size of 110μm. Reconstruction of data sets, PET/CT fusion and image analysis were done using IRW software (Siemens).

On day 21 after MI, cine MR images were obtained on a 7-Tesla Bruker Pharmascan with a custom-made mouse cardiac coil (Rapid Biomedical) and electrocardiogram and respiratory gating (SA Instruments). A gradient echo FLASH sequence had the following parameters: echo time 2.7 ms; 16 frames per R-R interval (repetition time 7.0 to 15.0 ms); in-plane resolution 200 μm × 200 μm × 1 mm; flip angle 60°; number of averages 4. Cardiac volumes were quantified from a stack of 6-8 short axis slices covering the entire left ventricle as described previously[25].

The MPO-sensitive MRI agent (MPO-Gd) was injected i.v. at a dose of 0.3 mmol/kg body weight 90 minutes prior to MRI. Images were analyzed with OsiriX DICOM viewer software (The Osirix Foundation). Signal intensities were measured by tracing a region of interest in the infarct, skeletal muscle, and outside the mouse. The contrast-to-noise ratio (CNR) was calculated as (target signal in infarct – skeletal muscle signal) / (standard deviation of the noise outside of animal).

Statistics

Results are expressed as mean ± SEM. Statistical comparisons between two groups were evaluated by Student's t-test. If more than 2 groups were compared we used ANOVA for multiple comparisons. We used GraphPad Prism 4.0c for Macintosh (GraphPad Software Inc.) for statistical analysis. P value of <0.05 was considered to be statistically significant.

RESULTS

Agent synthesis, pharmacokinetics and validation

We first established a protocol that allowed us to image infarct healing by PET/MRI. MPO-Gd served as a targeted molecular MRI agent because inflammatory Ly-6C^{high} monocytes express high amounts of MPO[26] and dominate the MR imaging signal in infarcts 90 minutes after injection of MPO-Gd, at a time when conventional Gd-DTPA has washed out[13]. To image extracellular matrix cross-linking by PET, we developed and validated a fluorine-18 version of a FXIII transglutaminase substrate peptide. To this end, we modified the lysine residue of the α_2-antiplasmin$_{13\text{-}24}$ substrate peptide[27] with the amine-reactive tetrazine linker to give FXIII-Tz with a yield of 66%. The radiolabeled prosthetic group ^{18}F-TCO was synthesized in 56% decay-corrected radiochemical yield. ^{18}F-TCO (≥ 94% pure after HPLC purification) and FXIII-Tz were then combined in a 'click' reaction resulting in ^{18}F-FXIII (Figure 1A). HPLC purification of the reaction mixture provided 2.8 ± 1.9 mCi of ^{18}F-FXIII in 58% decay-corrected radiochemical yield and >95% radiochemical purity (Figure 1B).

We injected ^{18}F-FXIII into B6 mice to measure the agent's blood-half life and biodistribution (n = 5). ^{18}F-FXIII had a blood half-life of 13.2 ± 0.94 minutes (R^2 = 0.95; Figure 1C). Biodistribution at 75 minutes after injection was as follows (expressed as %ID/g): liver, 2.83 ± 0.22; kidney, 1.26 ± 0.06; lymph node, 0.60 ± 0.1; spleen, 0.49 ± 0.05; blood, 0.49 ± 0.03; tail, 0.41 ± 0.03; skin, 0.31±0.05; bone, 0.31 ± 0.03; heart, 0.23 ± 0.03; intestines, 0.25 ± 0.04; fat, 0.17 ± 0.01; and muscle, 0.15 ± 0.01 (Figure 1D). To assess the presence of ^{18}F-FXIII in myocardial infarcts, we injected B6 mice with or without MI with ^{18}F-FXIII on day 4 after coronary ligation (n = 4-5 per group). Scintillation counting revealed that B6 mice with MI had significantly higher ^{18}F-FXIII signal in the heart compared to control mice (Figure 2A). Next, we assessed ^{18}F-FXIII specificity by injecting ^{18}F-FXIII into FXIII$^{-/-}$ mice with and without MI. Signal intensity in hearts of FXIII$^{-/-}$ mice with MI was significantly lower and comparable to non-infarcted wild-type B6 and FXIII$^{-/-}$ mice ($p<0.05$, Figure 2A). In B6 mice, TTC staining correlated pale infarct areas with enhanced ^{18}F-FXIII signal on autoradiography (Figure 2B). PET/MRI on day 4 after coronary ligation allowed assessment of transglutaminase activity by ^{18}F-FXIII and infarct inflammation with MPO-Gd (Figure 2C-E).

Monocytes are not a dominant source of infarct transglutaminase activity

The active subunit A of FXIII is synthesized in the bone marrow and circulates in plasma bound to the subunit B. Cellular FXIII lacks the B subunit and can be found in platelets and monocytes[28]. Transglutaminase activity in the infarct is crucial for wound healing, as even heterozygous FXIII deficient mice rupture their left ventricles[14]. One goal of our study was to reduce monocyte recruitment in apoE$^{-/-}$ mice in which blood monocytosis leads to

exaggerated and prolonged monocyte recruitment and impaired wound healing[7]. We therefore wondered to what degree monocytes contribute to transglutaminase activity in infarcts. If they contributed substantially, curbing monocyte recruitment may decrease FXIII activity and impair wound healing. To this extent, we measured FXIII activity in infarcts after systemic monocyte depletion with clodronate liposomes (Clo-Lip)[9] (n = 5 per group). We found no significant difference in FXIII activity in hearts of mice treated with Clo-Lip as compared to controls ($p>0.05$; Figure 3), suggesting that monocytes are not the primary source of FXIII in infarcts. These data imply that inhibition of monocyte recruitment does not decrease infarct transglutaminase activity.

Silencing of CCR2 mRNA ameliorates inflammation in MI

We next tested the hypothesis that dampening of Ly-6C^{high} monocyte recruitment improves infarct healing in apoE$^{-/-}$ mice. Indeed, flow cytometry analysis showed reduced presence of lineage^{-} CD11b^{+} myeloid cells ($p<0.05$) and inflammatory Ly-6C^{high} monocytes ($p<0.05$) in 4 day old infarcts of mice treated with siCCR2 (Figure 4A, B; n = 4 per group). Ly-6C^{low} monocytes were also reduced, and we observed a trend towards lower numbers of CD11b^{high} lineage^{high} neutrophils and F4/80^{+} macrophages in siCCR2 treated mice (Supplementary Figure 1). Quantitative reverse-transcriptase PCR (qRT-PCR) of infarcted myocardium assessed differential gene expression and clustering of treatment groups (Figure 4C and 4D). Systemic silencing of CCR2 reduced the expression of inflammatory genes, including CCR2, monocyte chemoattractant protein-1, myeloperoxidase, interleukin-6, interleukin-1β, nuclear factor kappa B, and tumor necrosis factor-α. Interleukin-10 and arginase gene expression increased (Figure 4C).

These findings were confirmed by immunoreactive staining on day 7 after MI. In mice treated with siCCR2, we found fewer Ly-6G^{+} neutrophils and CD11b^{+} myeloid cells compared to siCON treated controls (20.1±1.7 vs. 11.8±1.8 and 26.6±4.9 vs. 9.6±1.0 cells per high power field, respectively; $p<0.01$ for both; Figure 5A and 5B). Staining for α-SMA, collagen-1, and CD31 showed no difference between the two treatment cohorts (Figure 5C-E), suggesting that reduction of Ly-6C^{high} monocytes in apoE$^{-/-}$ mice did not adversely affect these wound healing biomarkers. Furthermore, CCR2 silencing did not have an adverse effect on the clearance of necrotic myocardium. On day 7 after MI, the residual necrotic debris within the infarct was lower in siCCR2 treated apoE$^{-/-}$ mice (Figure 6).

Dual-target molecular PET/MRI detects the therapeutic response to RNAi

Next we employed dual target molecular PET/MRI to monitor siCCR2 therapy in vivo, as non-invasive imaging of wound healing allowed us to assess left ventricular remodeling in the same mice with follow-up MRI volumetry. ApoE$^{-/-}$ mice were treated with siCCR2 or siCON on days 1 and 3 after MI (n = 5 per group). On day 4 after MI, PET/MRI with ^{18}F-FXIII and MPO-Gd revealed unchanged transglutaminase activity and decreased MPO activity in the infarct (Figure 7A). In an additional cohort of mice we measured mRNA levels of the FXIIIA subunit, which were unchanged by siCCR2 treatment and 10-fold lower than in the bone marrow (Supplementary Figure 2). The contrast-to-noise ratio on MPO-Gd MRI in siCCR2 treated mice was reduced by 75% ($p<0.05$, Figure 7B) when compared to siCON treated controls.

To investigate if the improved resolution of inflammation translates into attenuated ventricular remodeling, we measured cardiac volumes by cine MRI volumetry on day 21 after MI in the same cohorts that underwent PET/MRI on day 4. In apoE$^{-/-}$ mice treated with siCCR2, adverse remodeling was reduced, indicated by a lower end-diastolic volume, a lower end-systolic volume, and a higher left ventricular ejection fraction ($p<0.05$, Figure 8).

Discussion

Despite significant progress in the care for patients with myocardial infarction, the development of post-MI heart failure remains one of the biggest problems in cardiovascular medicine. It is increasingly understood that healing after MI offers a therapeutic opportunity to attenuate left ventricular remodeling, as this two-week scar-building process sets the stage for left ventricular remodeling in many patients[2, 4]. In the current work, we present two advances focusing on the acute healing phase after MI: i) We developed a new approach to follow infarct healing *in vivo* with dual-target PET/MRI for simultaneous monitoring of inflammation (i.e. tissue destruction) as well as tissue repair. ii) We report therapeutic effects of *in vivo* RNAi that targets the inflammatory monocyte subset.

Monocytes and their lineage-descendant macrophages are the most numerous leukocyte type in any wound, including the ischemic heart[6]. After injury, two distinct monocyte subsets accumulate in the infarct tissue[9]. The first to arrive are Ly-6C^{high} monocytes, which are rich in proteases and inflammatory cytokines. In wild type mice with undisturbed wound healing, their presence starts to wane 4 days after MI. Reparative Ly-6C^{low} monocytes dominate later wound healing stages during resolution of inflammation. These cells resemble non-classical macrophages, and may even give rise to them. The finely tuned healing response of the innate immune system derails if MI is induced in apoE$^{-/-}$ mice with pre-existing atherosclerotic disease[7]. In mice and humans, the same cells (monocytes and macrophages) are involved in atherosclerotic lesion development as well as in infarct healing. There is substantial crosstalk between the acute inflammation in the infarct and the chronic inflammation fueling plaque growth and destabilization[10, 29], leading to prolonged and exaggerated recruitment of inflammatory cells into the cardiac wound[7]. Interestingly, the kinetics of cell turn-over in ischemic myocardium are very rapid, even several days after the injury. The average residence time of a monocyte in the infarct is 20 hours, after which newly minted and recruited cells replace the previous generation of leukocytes[30]. The continuously high recruitment rates imply that monocyte supply, and especially recruitment, are potential therapeutic targets if one aims to diminish their numbers in tissue to curb inflammatory activity. Silencing the chemokine receptor CCR2 in apoE$^{-/-}$ mice lead to a decreased number of inflammatory cells in the infarct on day 4 after coronary ligation (41% reduction of Ly-6C^{high} monocytes), which correlated with a reduction in inflammatory gene expression in the infarct (see Figure 4), in line with data reported earlier for MCP-1[11] and CCR2$^{-/-}$ mice[31]. Of note, the silencing therapy may not be entirely specific to inflammatory monocytes, as other immune cells such as NK cells rely on CCR2 signaling for their recruitment[32]. In addition, we found that RNAi also reduced the number of other leukocytes such as neutrophils and Ly-6C^{low} monocytes. We speculate that these effects may have been caused by an overall dampened inflammatory activity, and reduction of the chemokines that recruit these cells. Supporting the resolution of inflammation in the first days after MI attenuated left ventricular dilation quantified 3 weeks later. Other wound healing biomarkers such as number of new vessels and the amount of collagen-1 in the scar were unaffected, possibly because silencing CCR2 targets monocytes without affecting activity of endothelial cells and fibroblasts.

Off-target effects and the challenge of siRNA delivery to the appropriate tissue are the main obstacles to therapeutic *in vivo* silencing. In our study, control cohorts received irrelevant siRNA to neutralize off-target effects. Modification of siRNA and delivery by nanoparticles have taken some of these hurdles[33]. Toxicity and pro-inflammatory properties were diminished while silencing potency increased, reducing the dose necessary to achieve therapeutic effects. As a result, clinical trials targeting hepatocytes are under way, one of them reducing LDL cholesterol levels by silencing PCSK9[34, 35]. Studies in non-human

primates show that targets in leukocytes are not off-limits in higher species[36], and that the approach used in this study has translational potential.

Imaging to monitor infarct healing in this study used a hybrid approach to follow the therapeutic target (inflammatory leukocytes) in conjunction with an additional biomarker that reports on potential 'collateral damage' of anti-inflammatory therapy in wound healing (plasma transglutaminase). Myeloperoxidase is most abundant in neutrophils and inflammatory monocytes[26], the cell types that should decrease in presence during resolution of inflammation. MPO-Gd MRI reported reduced infarct myeloperoxidase activity in the infarct after siCCR2 treatment, in line with ex vivo data that showed effective reduction of myeloperoxidase-rich Ly-6C^{high} monocytes and neutrophils. Recently, the first clinical cardiac cellular MRI studies followed monocyte/macrophage presence in infarcts of human patients with iron oxide nanoparticles[37, 38]. This approach could also be used to follow therapeutic efficacy, albeit these nanoparticles may not be able to differentiate between monocyte subsets. The PET component in our study reported on FXIII activity. The alpha subunit of plasma transglutaminase forms covalent bonds between peptide chains. In the coagulation cascade, FXIII is a downstream clotting factor that cross-links fibrin monomers[28]. In a healing infarct, FXIII cross-links extracellular matrix, among other functions[28]. The importance of the imaged enzyme in wound healing is highlighted by a 100% infarct rupture rate in heterozygous FXIII deficient mice[14]. Decreased FXIII activity in patients associates with impaired wound healing[28]. We here developed a fluorine-18 labeled substrate peptide for PET imaging, building on previous work that established and validated this concept for other imaging modalities[14, 15]. The combination of myeloperoxidase-targeted MRI and FXIII-targeted PET highlights the potential of cardiac PET/MRI[39, 40], as it simultaneously quantifies inflammation and tissue repair, key aspects of infarct healing that are likely interconnected. For instance, one could speculate that if the MPO MRI signal increases due to unresolved inflammatory activity, transglutaminase signal may decrease, because disturbed inflammation resolution hinders repair and matrix generation. We used this imaging strategy to follow a therapeutic intervention which reduced inflammation in mice with impaired infarct healing due to blood monocytosis with PET/MRI. The advent of MRI-compatible silicon avalanche photodiode PET detectors fostered integration of both modalities within one system. While our study used off-line data fusion after acquisition in separate scanners, it showcases the opportunities provided by molecular PET/MRI[40]. The MRI component could potentially also report on infarct size, edema, tissue deformation, and perfusion[41-44]; and correlate these to molecular data obtained by PET[45-48].

In conclusion, our study presents two advances: we found that targeting inflammatory monocytes with RNAi during infarct healing attenuated left ventricular dilation and reduced post-MI heart failure in mice. Further, we combined this therapy with companion molecular imaging that followed the treatment response in parallel with possible side- or downstream effects by PET/MRI. This imaging strategy is clinically translatable and presents an opportunity to closely monitor sequela of interfering with the immune system, which requires caution because innate immune cells have not only disease-promoting but also protective effects.

Supplementary Material

Refer to Web version on PubMed Central for supplementary material.

Acknowledgments

We gratefully acknowledge the Alnylam medium scale synthesis group for preparing the CCR2 siRNA, Will Cantley for making the liposomal formulation, Cuihua Wang for MPO-Gd synthesis, and Victor Koteliansky and Tatiana Novobrantseva for helpful discussions.

Sources of Funding This project has been funded in part with Federal funds from the National Heart, Lung, and Blood Institute, National Institutes of Health, Department of Health and Human Services, under Contract No. HHSN268201000044C, and grants R01-HL096576, R01-HL095629, and T32-HL094301. T.H. was funded by Deutsche Forschungsgemeinschaft HE-6382/1-1.

References

1. Frangogiannis NG, Smith CW, Entman ML. The inflammatory response in myocardial infarction. Cardiovasc Res. 2002; 53:31–47. [PubMed: 11744011]
2. Frantz S, Bauersachs J, Ertl G. Post-infarct remodelling: contribution of wound healing and inflammation. Cardiovasc Res. 2009; 81:474–481. [PubMed: 18977766]
3. Lambert JM, Lopez EF, Lindsey ML. Macrophage roles following myocardial infarction. Int J Cardiol. 2008; 130:147–158. [PubMed: 18656272]
4. French BA, Kramer CM. Mechanisms of Post-Infarct Left Ventricular Remodeling. Drug Discov Today Dis Mech. 2007; 4:185–196. [PubMed: 18690295]
5. Lindsey ML, Mann DL, Entman ML, Spinale FG. Extracellular matrix remodeling following myocardial injury. Ann Med. 2003; 35:316–326. [PubMed: 12952018]
6. Nahrendorf M, Pittet MJ, Swirski FK. Monocytes: protagonists of infarct inflammation and repair after myocardial infarction. Circulation. 2010; 121:2437–2445. [PubMed: 20530020]
7. Panizzi P, Swirski FK, Figueiredo JL, Waterman P, Sosnovik DE, Aikawa E, Libby P, Pittet M, Weissleder R, Nahrendorf M. Impaired infarct healing in atherosclerotic mice with Ly-6C(hi) monocytosis. J Am Coll Cardiol. 2010; 55:1629–1638. [PubMed: 20378083]
8. Robbins CS, Chudnovskiy A, Rauch PJ, Figueiredo JL, Iwamoto Y, Gorbatov R, Etzrodt M, Weber GF, Ueno T, van Rooijen N, Mulligan-Kehoe MJ, Libby P, Nahrendorf M, Pittet MJ, Weissleder R, Swirski FK. Extramedullary hematopoiesis generates Ly-6C(high) monocytes that infiltrate atherosclerotic lesions. Circulation. 2012; 125:364–374. [PubMed: 22144566]
9. Nahrendorf M, Swirski FK, Aikawa E, Stangenberg L, Wurdinger T, Figueiredo JL, Libby P, Weissleder R, Pittet MJ. The healing myocardium sequentially mobilizes two monocyte subsets with divergent and complementary functions. J Exp Med. 2007; 204:3037–3047. [PubMed: 18025128]
10. Swirski FK, Nahrendorf M. Leukocyte behavior in atherosclerosis, myocardial infarction, and heart failure. Science. 2013; 339:161–166. [PubMed: 23307733]
11. Dewald O, Zymek P, Winkelmann K, Koerting A, Ren G, Abou-Khamis T, Michael LH, Rollins BJ, Entman ML, Frangogiannis NG. CCL2/Monocyte Chemoattractant Protein-1 regulates inflammatory responses critical to healing myocardial infarcts. Circ Res. 2005; 96:881–889. [PubMed: 15774854]
12. Leuschner F, Dutta P, Gorbatov R, Novobrantseva TI, Donahoe JS, Courties G, Lee KM, Kim JI, Markmann JF, Marinelli B, Panizzi P, Lee WW, Iwamoto Y, Milstein S, Epstein-Barash H, Cantley W, Wong J, Cortez-Retamozo V, Newton A, Love K, Libby P, Pittet MJ, Swirski FK, Koteliansky V, Langer R, Weissleder R, Anderson DG, Nahrendorf M. Therapeutic siRNA silencing in inflammatory monocytes in mice. Nat Biotechnol. 2011; 29:1005–1010. [PubMed: 21983520]
13. Nahrendorf M, Sosnovik D, Chen JW, Panizzi P, Figueiredo JL, Aikawa E, Libby P, Swirski FK, Weissleder R. Activatable magnetic resonance imaging agent reports myeloperoxidase activity in healing infarcts and noninvasively detects the antiinflammatory effects of atorvastatin on ischemia-reperfusion injury. Circulation. 2008; 117:1153–1160. [PubMed: 18268141]
14. Nahrendorf M, Hu K, Frantz S, Jaffer FA, Tung CH, Hiller KH, Voll S, Nordbeck P, Sosnovik D, Gattenlohner S, Novikov M, Dickneite G, Reed GL, Jakob P, Rosenzweig A, Bauer WR, Weissleder R, Ertl G. Factor XIII deficiency causes cardiac rupture, impairs wound healing, and

aggravates cardiac remodeling in mice with myocardial infarction. Circulation. 2006; 113:1196–1202. [PubMed: 16505171]

15. Jaffer FA, Tung CH, Wykrzykowska JJ, Ho NH, Houng AK, Reed GL, Weissleder R. Molecular imaging of factor XIIIa activity in thrombosis using a novel, near-infrared fluorescent contrast agent that covalently links to thrombi. Circulation. 2004; 110:170–176. [PubMed: 15210587]
16. Keliher EJ, Reiner T, Turetsky A, Hilderbrand SA, Weissleder R. High-yielding, two-step 18F labeling strategy for 18F-PARP1 inhibitors. ChemMedChem. 2011; 6:424–427. [PubMed: 21360818]
17. Selvaraj R, Liu S, Hassink M, Huang CW, Yap LP, Park R, Fox JM, Li Z, Conti PS. Tetrazine-trans-cyclooctene ligation for the rapid construction of integrin alphavbeta(3) targeted PET tracer based on a cyclic RGD peptide. Bioorg Med Chem Lett. 2011; 21:5011–5014. [PubMed: 21601452]
18. Han HS, Devaraj NK, Lee J, Hilderbrand SA, Weissleder R, Bawendi MG. Development of a bioorthogonal and highly efficient conjugation method for quantum dots using tetrazine-norbornene cycloaddition. J Am Chem Soc. 2010; 132:7838–7839. [PubMed: 20481508]
19. Keliher E, Reiner T, Thurber GM, Upadhay R, Weissleder R. Efficient 18F-Labeling of Synthetic Exendin-4 Analogues for Imaging Beta Cells. Chemistry Open. 2012; 1:177–183.
20. Querol M, Chen JW, Weissleder R, Bogdanov AJ. DTPA-bisamide-based MR sensor agents for peroxidase imaging. Org Lett. 2005; 7:1719–1722. [PubMed: 15844889]
21. Chen JW, Querol Sans M, Bogdanov AJ, Weissleder R. Imaging of myeloperoxidase in mice by using novel amplifiable paramagnetic substrates. Radiology. 2006; 240:473–481. [PubMed: 16864673]
22. Chen JW, Breckwoldt MO, Aikawa E, Chiang G, Weissleder R. Myeloperoxidase-targeted imaging of active inflammatory lesions in murine experimental autoimmune encephalomyelitis. Brain. 2008; 131:1123–1133. [PubMed: 18234693]
23. Rodriguez E, Nilges M, Weissleder R, Chen JW. Activatable magnetic resonance imaging agents for myeloperoxidase sensing: mechanism of activation, stability, and toxicity. J Am Chem Soc. 2010; 132:168–177. [PubMed: 19968300]
24. Lee WW, Marinelli B, van der Laan AM, Sena BF, Gorbatov R, Leuschner F, Dutta P, Iwamoto Y, Ueno T, Begieneman MP, Niessen HW, Piek JJ, Vinegoni C, Pittet MJ, Swirski FK, Tawakol A, Di Carli M, Weissleder R, Nahrendorf M. PET/MRI of inflammation in myocardial infarction. J Am Coll Cardiol. 2012; 59:153–163. [PubMed: 22222080]
25. Yang Z, Berr SS, Gilson WD, Toufektsian MC, French BA. Simultaneous evaluation of infarct size and cardiac function in intact mice by contrast-enhanced cardiac magnetic resonance imaging reveals contractile dysfunction in noninfarcted regions early after myocardial infarction. Circulation. 2004; 109:1161–1167. [PubMed: 14967719]
26. Swirski FK, Wildgruber M, Ueno T, Figueiredo JL, Panizzi P, Iwamoto Y, Zhang E, Stone JR, Rodriguez E, Chen JW, Pittet MJ, Weissleder R, Nahrendorf M. Myeloperoxidase-rich Ly-6C+ myeloid cells infiltrate allografts and contribute to an imaging signature of organ rejection in mice. J Clin Invest. 2010; 120:2627–2634. [PubMed: 20577051]
27. Tung CH, Ho NH, Zeng Q, Tang Y, Jaffer FA, Reed GL, Weissleder R. Novel factor XIII probes for blood coagulation imaging. Chembiochem. 2003; 4:897–899. [PubMed: 12964167]
28. Muszbek L, Bereczky Z, Bagoly Z, Komaromi I, Katona E. Factor XIII: a coagulation factor with multiple plasmatic and cellular functions. Physiol Rev. 2011; 91:931–972. [PubMed: 21742792]
29. Dutta P, Courties G, Wei Y, Leuschner F, Gorbatov R, Robbins CS, Iwamoto Y, Thompson B, Carlson AL, Heidt T, Majmudar MD, Lasitschka F, Etzrodt M, Waterman P, Waring MT, Chicoine AT, van der Laan AM, Niessen HW, Piek JJ, Rubin BB, Butany J, Stone JR, Katus HA, Murphy SA, Morrow DA, Sabatine MS, Vinegoni C, Moskowitz MA, Pittet MJ, Libby P, Lin CP, Swirski FK, Weissleder R, Nahrendorf M. Myocardial infarction accelerates atherosclerosis. Nature. 2012; 487:325–329. [PubMed: 22763456]
30. Leuschner F, Rauch PJ, Ueno T, Gorbatov R, Marinelli B, Lee WW, Dutta P, Wei Y, Robbins C, Iwamoto Y, Sena B, Chudnovskiy A, Panizzi P, Keliher E, Higgins JM, Libby P, Moskowitz MA, Pittet MJ, Swirski FK, Weissleder R, Nahrendorf M. Rapid monocyte kinetics in acute myocardial

infarction are sustained by extramedullary monocytopoiesis. J Exp Med. 2012; 209:123–137. [PubMed: 22213805]

31. Kaikita K, Hayasaki T, Okuma T, Kuziel WA, Ogawa H, Takeya M. Targeted deletion of CC chemokine receptor 2 attenuates left ventricular remodeling after experimental myocardial infarction. Am J Pathol. 2004; 165:439–447. [PubMed: 15277218]
32. van Helden MJ, Zaiss DM, Sijts AJ. CCR2 Defines a Distinct Population of NK Cells and Mediates Their Migration during Influenza Virus Infection in Mice. PLoS One. 2012; 7:e52027. [PubMed: 23272202]
33. Whitehead KA, Langer R, Anderson DG. Knocking down barriers: advances in siRNA delivery. Nat Rev Drug Discov. 2009; 8:129–138. [PubMed: 19180106]
34. Frank-Kamenetsky M, Grefhorst A, Anderson NN, Racie TS, Bramlage B, Akinc A, Butler D, Charisse K, Dorkin R, Fan Y, Gamba-Vitalo C, Hadwiger P, Jayaraman M, John M, Jayaprakash KN, Maier M, Nechev L, Rajeev KG, Read T, Rohl I, Soutschek J, Tan P, Wong J, Wang G, Zimmermann T, de Fougerolles A, Vornlocher HP, Langer R, Anderson DG, Manoharan M, Koteliansky V, Horton JD, Fitzgerald K. Therapeutic RNAi targeting PCSK9 acutely lowers plasma cholesterol in rodents and LDL cholesterol in nonhuman primates. Proc Natl Acad Sci U S A. 2008; 105:11915–11920. [PubMed: 18695239]
35. Fitzgerald K, Frank-Kamenetsky M, Mant T, Ritter J, Chiesa J, Munasamy M, Hutabarat R, Clausen V, Watkins D, Smith K, Sutherland J, Cehelsky J, Kretschmer M, Nechev L, Karsten V, Nochur S, Binne L, Vaishnaw A, Simon A. Phase I Safety, Pharmacokinetic, and Pharmacodynamic Results for ALN-PCS, a Novel RNAi Therapeutic for the Treatment of Hypercholesterolemia. ATVB. 2012; 32:A67.
36. Novobrantseva TI, Borodovsky A, Wong J, Klebanov B, Zafari M, Yucius K, Querbes W, Ge P, Ruda VM, Milstein S, Speciner L, Duncan R, Barros S, Basha G, Cullis P, Akinc A, Donahoe JS, Narayanannair Jayaprakash K, Jayaraman M, Bogorad RL, Love K, Whitehead K, Levins C, Manoharan M, Swirski FK, Weissleder R, Langer R, Anderson DG, de Fougerolles A, Nahrendorf M, Koteliansky V. Systemic RNAi-mediated Gene Silencing in Nonhuman Primate and Rodent Myeloid Cells. Mol Ther Nucleic Acids. 2012; 1:e4. [PubMed: 23344621]
37. Mulder WJ, Griffioen AW, Strijkers GJ, Cormode DP, Nicolay K, Fayad ZA. Magnetic and fluorescent nanoparticles for multimodality imaging. Nanomedicine (Lond). 2007; 2:307–324. [PubMed: 17716176]
38. Alam SR, Shah AS, Richards J, Lang NN, Barnes G, Joshi N, Macgillivray T, McKillop G, Mirsadraee S, Payne J, Fox KA, Henriksen P, Newby DE, Semple SI. Ultrasmall Superparamagnetic Particles of Iron Oxide in Patients with Acute Myocardial Infarction: Early Clinical Experience. Circ Cardiovasc Imaging. 2012; 5:559–565. [PubMed: 22875883]
39. Marwick TH, Schwaiger M. The future of cardiovascular imaging in the diagnosis and management of heart failure, part 1: tasks and tools. Circ Cardiovasc Imaging. 2008; 1:58–69. [PubMed: 19808515]
40. Martinez-Moller A, Eiber M, Nekolla SG, Souvatzoglou M, Drzezga A, Ziegler S, Rummeny EJ, Schwaiger M, Beer AJ. Workflow and Scan Protocol Considerations for Integrated Whole-Body PET/MRI in Oncology. J Nucl Med. 2012; 53:1415–26. [PubMed: 22879079]
41. Kramer CM, Sinusas AJ, Sosnovik DE, French BA, Bengel FM. Multimodality imaging of myocardial injury and remodeling. J Nucl Med. 2010; 51(Suppl 1):107S–121S. [PubMed: 20395347]
42. Rehwald WG, Wagner A, Sievers B, Kim RJ, Judd RM. Cardiovascular MRI: its current and future use in clinical practice. Expert Rev Cardiovasc Ther. 2007; 5:307–321. [PubMed: 17338674]
43. Vandsburger MH, Epstein FH. Emerging MRI methods in translational cardiovascular research. J Cardiovasc Transl Res. 2011; 4:477–492. [PubMed: 21452060]
44. Dall'Armellina E, Karamitsos TD, Neubauer S, Choudhury RP. CMR for characterization of the myocardium in acute coronary syndromes. Nat Rev Cardiol. 2010; 7:624–636. [PubMed: 20856263]
45. Bravo PE, Bengel FM. The role of cardiac PET in translating basic science into the clinical arena. J Cardiovasc Transl Res. 2011; 4:425–436. [PubMed: 21573964]

46. Dobrucki LW, Sinusas AJ. PET and SPECT in cardiovascular molecular imaging. Nat Rev Cardiol. 2010; 7:38–47. [PubMed: 19935740]

47. Knuuti J, Bengel FM. Positron emission tomography and molecular imaging. Heart. 2008; 94:360–367. [PubMed: 18276820]

48. Sanz J, Fayad ZA. Imaging of atherosclerotic cardiovascular disease. Nature. 2008; 451:953–957. [PubMed: 18288186]

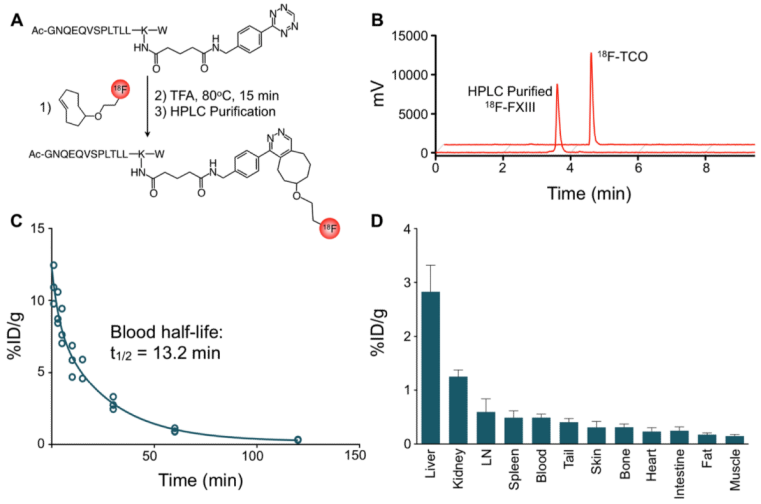

Figure 1. ^{18}F-FXIII PET agent

A, Schematic representation of agent synthesis. Factor XIII-tetrazine (FXIII-Tz) was reacted with prosthetic group ^{18}F-*trans*-cyclooctene (^{18}F-TCO) to give ^{18}F-FXIII. **B**, Analytical HPLC chromatographs ^{18}F-TCO and ^{18}F-FXIII following preparative scale HPLC purification. **C**, Blood half-life of ^{18}F-FXIII (n=5). **D**, Biodistribution of ^{18}F-FXIII PET agent 75 minutes after intravenous administration (n=5). Data are presented as mean±SEM.

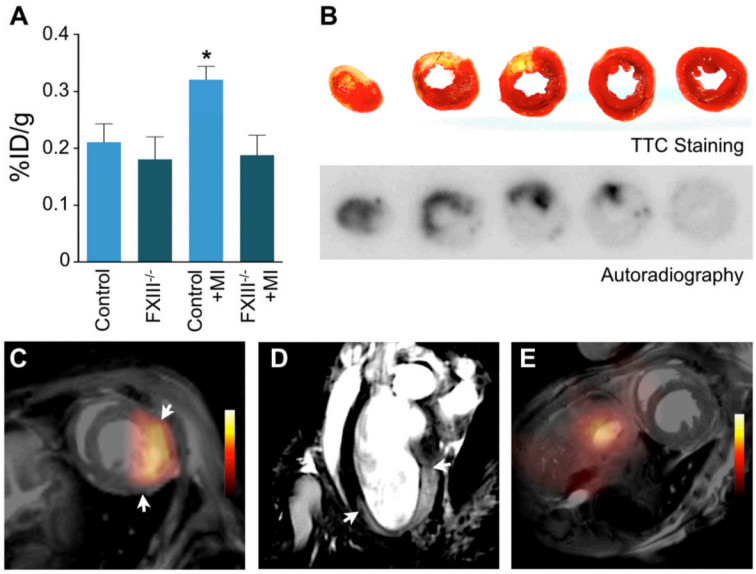

Figure 2. ^{18}F-FXIII/MPO-Gd PET/MRI in MI

A, Scintillation counting in hearts of control B6 mice with and without MI compared to FXIII$^{-/-}$ mice (day 4 after MI, n=4-5 per group). Data are mean±SEM, *p<0.05; p-value was tested between B6 mice with MI and control B6 mice. **B**, TTC staining of infarcted tissue (yellow) and viable myocardium (red) correlated with ^{18}F-FXIII signal on autoradiography in B6 mouse on day 4 after MI. **C-D**, *In vivo* dual target molecular PET/MRI of wound healing and myocardial inflammation in a wild type B6 mouse on day 4 after coronary ligation. The short axis (C) shows ^{18}F-FXIII PET signal in MI fused to MR image. A representative long axis MR image (D) shows signal enhancement in the infarct area 90 minutes after intravenous MPO-Gd injection. Arrows indicate infarct borders. **E**, PET/MRI of control mouse without coronary ligation.

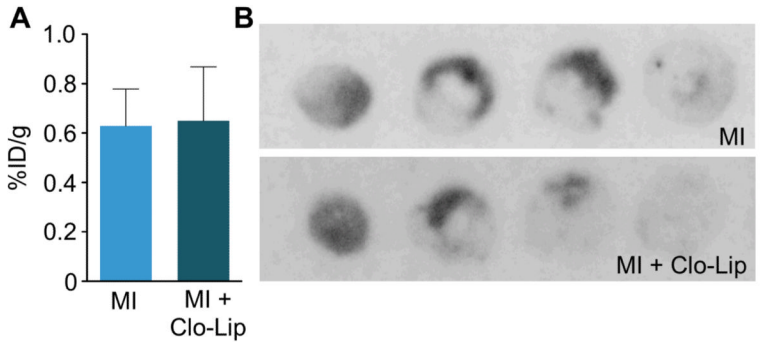

Figure 3. Monocytes are not a major source of FXIII in MI

A, Scintillation counting of infarcted hearts from mice with or without clodronate liposome (Clo-Lip) depletion of monocytes and macrophages after injection of ^{18}F-FXIII (n=4-5 per group). **B**, Comparison of ^{18}F-FXIII signal on autoradiography between control mouse (MI) and mouse treated with Clo-Lip (MI + Clo-Lip). Data are mean±SEM, *p<0.05. %ID/g: percent injected dose per gram tissue.

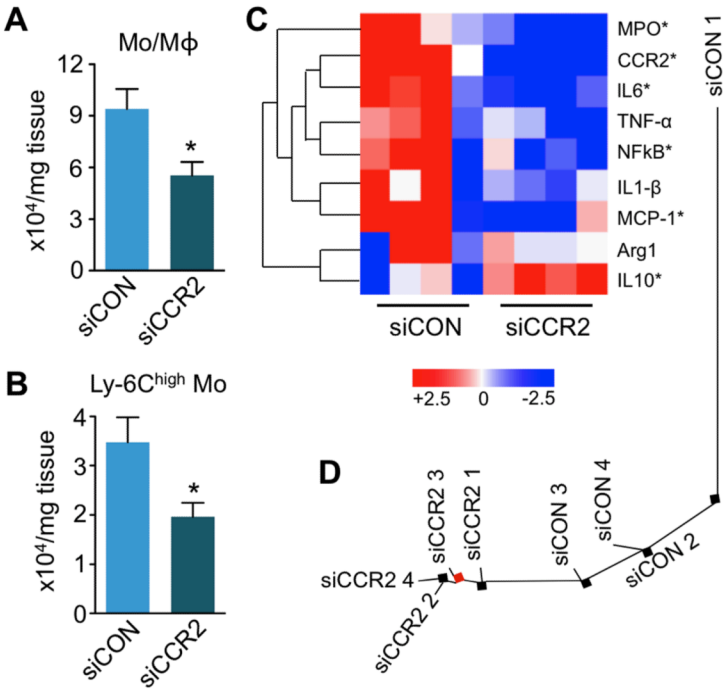

Figure 4. Treatment with siCCR2 reduces inflammatory monocytes in the heart

A, Flow cytometric analysis of 4 day old infarcts shows decreased $CD11b^{+}$ $lineage^{-}$ myeloid cells (Mo/Mϕ). Dot plots and gating strategy are shown in supplementary Figure 1. **B**, Number of Ly-$6C^{high}$ monocytes in infarcts. Data are mean±SEM, n=4 per group, *p<0.05. **C**, Heat map of genes in infarcted myocardium (n=4 per group). Each row of the heat map represents a gene while each column represents an experimental treatment group (labeled at the bottom). The color scale represents the level of gene expression, with red indicating an increase in gene expression and blue indicating a decrease in gene expression. Data underwent z-score transformation for display. **D**, Distance tree showing the relative location and clustering of treatment cohorts.

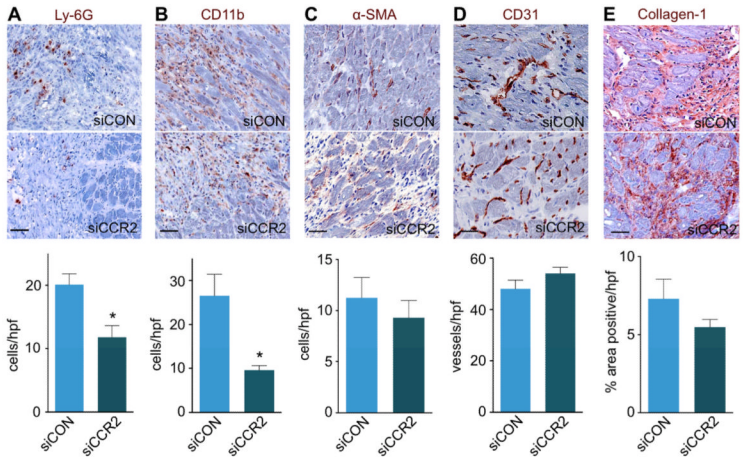

Figure 5. siCCR2 treatment effects on wound healing

A-E, Immunohistochemical evaluation of the infarct after siCCR2 or siCON treatment for neutrophils (**A**, Ly-6G), myeloid cells (**B**, CD11b), myofibroblasts (**C**, α-SMA), neovessels (**D**, CD31), and collagen deposition (E, collagen-1). Images depict border zone of the infarct. n=4 mice per group and n=4 high power fields (hpf) /mouse. Data are mean±SEM, *p<0.05. Scale bar indicates 25μm.

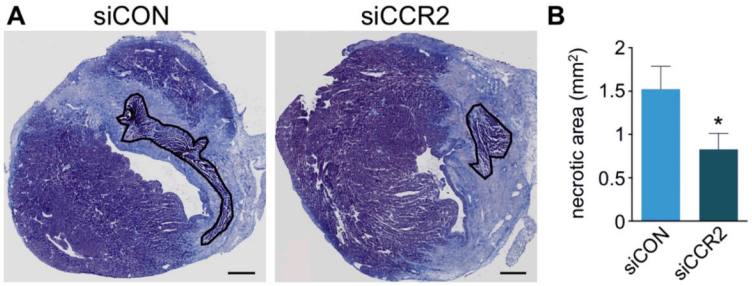

Figure 6. CCR2 silencing reduces residual necrotic debris

A, Masson trichrome stain with residual necrotic debris in infarct outlined in black. **B**, Comparison of residual necrotic debris between siCON and siCCR2 treated animals (4 mice per group). Data are mean±SEM, *p<0.05. Scale bar indicates 0.5 mm.

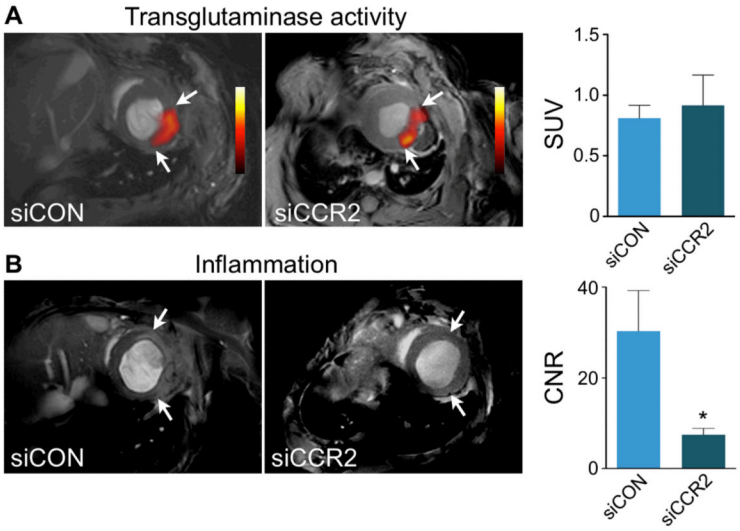

Figure 7. Dual target molecular PET/MRI after therapeutic RNA silencing of CCR2

A, Short axis PET/MRI images after respective siRNA treatment. Bar graph of standard uptake value (SUV) shows no difference in ^{18}F-FXIII PET signal between treatment groups (n=5 per group). **B**, Short axis MRI showing MPO-Gd signal enhancement in siCON and reduced enhancement in siCCR2 treated mice. Arrows indicate infarct area. The bar graph shows contrast-to-noise ratio (CNR). Data are mean±SEM, *p<0.05.

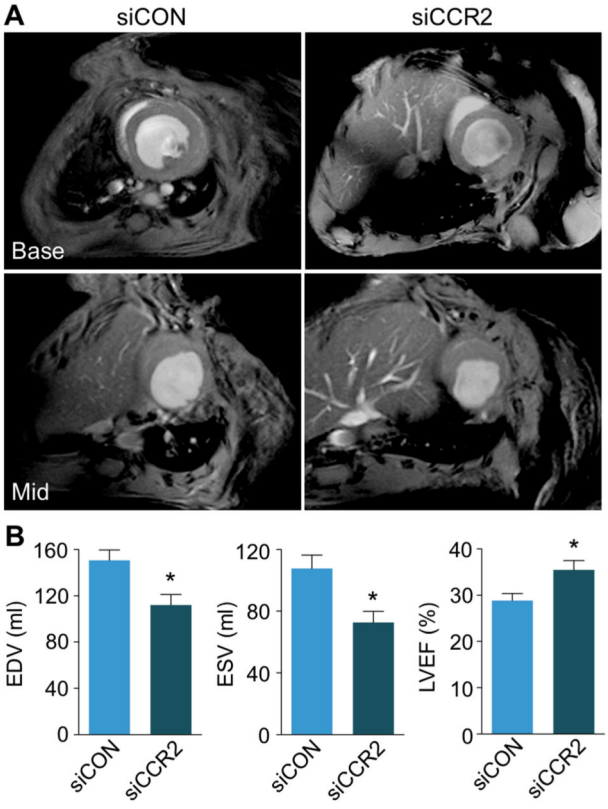

Figure 8. CCR2 silencing reduces adverse ventricular remodeling

A, Basal and mid-ventricular short axis cine MR images on day 21 after MI. **B**, Bar graphs depict differences in left ventricular remodeling between siCON and siCCR2 treated cohorts (n=5 per group). Data are mean±SEM, *p<0.05. EDV: end-diastolic volume; ESV: end-systolic volume; LVEF: left ventricular ejection fraction.